Supplementary information for

RGD/CTX-Conjugated Multifunctional Eu-Gd_2O_3 NRs for Targeting Detection and Inhibition of Early Tumor

Zhi Wu[a], Zhongbing Huang[a*], Guangfu Yin[a], Bianyun Cai[a], Lei Wang[b], Fabao Gao[b*]

[a] College of Materials Science and Engineering, Sichuan University, Chengdu, 610065, China. *Email: zbhuang@scu.edu.cn; Fax: 86-28-85413003; Tel: 86-28-85413003

[b] Molecular Imaging Center, Department of Radiology, West China Hospital of Sichuan University, No. 2, 4th Keyuan Road, Chengdu 610093, China. *Email: gaofabao@yahoo.com

1. Experimental Sections

1.1. Characterization

The crystal structure was examined by DX-1000 diffractometer (Dandong Fangyuan Instrument Co. Itd., Cu Kα radiation, λ = 1.5418, 40 kV, 80 mA), with a step size of 0.6°. The morphology was observed with a field emission scanning electron microscope (SEM, JEOL-5900LV, 20 kV, Japan). The zeta−potential values were measured by zeta-sizer (Malvern, Nano ZS). The Ultra-Violet (UV) absorption patterns were obtained with a Spectrophotometer (U-3010, Hitachi, Japan). X-ray photoelectron spectroscopy (XPS) patterns were obtained with a Scanning X-ray Microprobe^{TM} (ΦULVAC-PHI. INC.). Thermogravimetry (TG) was carried out with a TG/SDTA851^{e} analyzer (METTLER-TOLEDO Co. Switzerland) in air at the heating rate of 10 ^{o}C/min in the range of room temperature (RT) ~ 800 ^{o}C. The fluorescence was analyzed using a Fluorescence Spectrophotometer (F-7000, Japan), and the fluorescence photographs of Eu-Gd_2O_3 NRs dispersed in deionized water were taken with a FUJIFILE digital camera.

1.2. Ninhydrin reaction assay

As reported, ninhydrin could effectively detect the existence of amino groups *via* chemical reaction. In detail, 30 mg of aminated Eu-Gd_2O_3 NRs obtained at different temperature (RT ~ 90 ^{o}C) were dispersed in 6 mL of deionized water in glass tubes, respectively. After 500 μL of ninhydrin solution was added, the NRs-dispersed solution in glass tubes were boiled for 15 min. Finally, the reacted liquid was photographed, and the supernatant after centrifugation was analyzed with UV absorption of a Spectrophotometer (U-3010, Hitachi, Japan).

1.3. Cells culture

U251 cells (human glioblastoma cells), human umbilical vein endothelial cells (HUVECs) and fibroblast cells (L929) were cultured, respectively, in Dulbecco's Modified Eagle Medium (DMEM, Gibco) supplemented with 10% fetal bovine serum (FBS, Gibco), 100 U·mL^{-1} penicillin and 100 mg·mL^{-1} streptomycin at 37 ^{o}C under 5% CO_2.

1.4. *In vitro* cytotoxicity investigation

The cytotoxicity of the as-prepared pure NRs and PEG-NRs with various concentrations was investigated by a 3-(4,5-dimethylthiazol-2-yl)-2,5-diphenyltetrazolium bromide (MTT) assay with L929 cells, HUVECs and U251 cells, respectively. The cells were cultured as ***Section 1.3.*** 100 μL of cells suspension (5×10^4 cells·mL^{-1}) was seeded into a 96-well plate (BD Biosciences) and incubated at 37 ^{o}C and 5% CO_2 for 24 h. After the cells were adhered, the disinfected pure NRs or PEG-NRs were added into the wells at different concentrations (25 ~ 200 μg·mL^{-1} of NRs). The wells without NRs were as control. The cells were subsequently incubated for 2 d at 37 ^{o}C and 5% CO_2. After washed three times with PBS solution, and added by 100 μL of medium, the cells were observed under an inverted fluorescence microscopy (IFM, IX71, Olympus, Japan) at a magnification of 200 ×. Then, MTT solution was added (20 μL per well) and the cells were further incubated for 4 h. Finally, the medium in the wells was removed and 150 μL of DMSO was added into each well. Absorbance of solubilized formazan at 490 nm was measured by Microplate Reader 3550 (Bio-Rad). The cell viability was calculated by the following formula: cell viability (%) = [optical density (OD) of the treated cells – OD of the NRs] / OD of the control cells. All of the experiments were performed in triplicate.

Data are expressed as means ± standard deviations (SD) of a representative of three similar experiments performed in triplicate. Statistical analysis was carried out with the statistical package for the social sciences (SPSS). Least-significant difference and Tukey tests were used to evaluate their differences between the test group and the control, and $p < 0.05$ and $p < 0.01$ were considered as the statistical significance.

1.5. Animal administration

Kunming mice (~ 30 g), Sprague Dawley rats (SD rats, ~ 200 g) were purchased from Laboratory Animal Center of Sichuan University (Chengdu, China). All animals procedures were in accord with the guidelines of the Institutional Animal Care and Use Committee. To avoid the pregnancy during the test, all the used mice were male.

1.6. Hemolysis Test *in vitro*

Hemolysis test was carried out as an important factor to evaluate the biocompatibility of nanomaterials *in vitro*. Blood samples were obtained from SD rats through cardiac puncture after SD rats were euthanized with 200 μL of 10% chloral hydrate (dissolved in PBS solution) *via* intraperitoneal injection and stabilized by saturated EDTA solution (dissolved in PBS solution).

First, 1 mL of blood sample was added to 2 mL of PBS solution (pH = 7.2), and centrifuged (8000 rpm) for 10 min to obtain the red blood cells (RBCs). After washed five times with 5 mL of PBS solution, the purified blood sample was diluted to 1/10 of its volume with PBS solution. 0.2 mL of diluted RBCs suspension was then mixed with (a) 0.8 mL of PBS solution as the negative control, (b) 0.8 mL of deionized water as the positive control, and (c) 0.8 mL of Eu-Gd_2O_3 NRs and PEG-NRs suspensions at concentrations ranging from 0 ~ 1000 $\mu g \cdot mL^{-1}$ as the test groups. Then, all the mixtures were oscillated and kept at 37 ^oC for 3 h. Finally, the mixtures were centrifuged (12000 rpm) for 5 min, the absorbance of supernatants at 541 nm was measured by a Microplate Reader 3550 (Bio-Rad). The percentage of hemolysis of RBCs was calculated as following: the percentage of hemolysis (%) = [(sample absorbance – negative control absorbance) / (positive control absorbance – negative control absorbance)] × 100.

1.7. Histology analysis, bio-distribution and toxicity *in vivo*

For histology analysis and bio-distribution, Kunming mice were sacrificed through euthanizing with 200 μL of 10% chloral hydrate (dissolved in PBS solution) *via* intraperitoneal injection for 1 d after tail-vein injected with pure NRs, PEG-NRs, RGD-NRs, CTX-NRs and RGD-NRs-CTX at a concentration of 10 mg Gd/kg rats, respectively. The heart, liver, spleen, lung and kidney from NRs-injected mice were collected and washed with 0.9 wt% physiological saline 5 times, especially the lungs, to remove the residual blood farthest. Subsequently, on the one hand, half of each organ was weighted and boiled in a digestion solution of mixed acids (nitric acid : perchloric acid, v : v = 3 : 1) for 1 h, and Gd ion concentrations in these digestion solutions were determined by inductively coupled plasma atomic emission spectrometer (ICP-AES, SPECTRO ARCOS, Germany). Kunming mice untreated with NRs were used as the control. Gd ion contents of various organs from mice were calculated, based on the control as the percentage of injected dose per gram

of wet tissues (ID%/g)[1]. On the other hand, the residual part of each organ was fixed in 4 wt% buffered paraformaldehyde for 48 h, dehydrated in ethanol, and embedded in paraffin for slides preparation. The slices of these organs were stained with hematoxylin and eosin (H & E) and observed under an inverted flurorescence microscopy (IFM) at a magnification of 100 ×. For long-term toxicity, the weights/day of mice were recorded persistently for 10 d after their administration with the five different NRs at the concentration of 10 mg Gd/kg rats, and mice treated with the same amount of 0.9 wt.% physiological saline were as the control group. Finally, the mice were sacrificed by the same way and their organs were collected to analyze the bio-distribution and histology toxicity of the injected NRs.

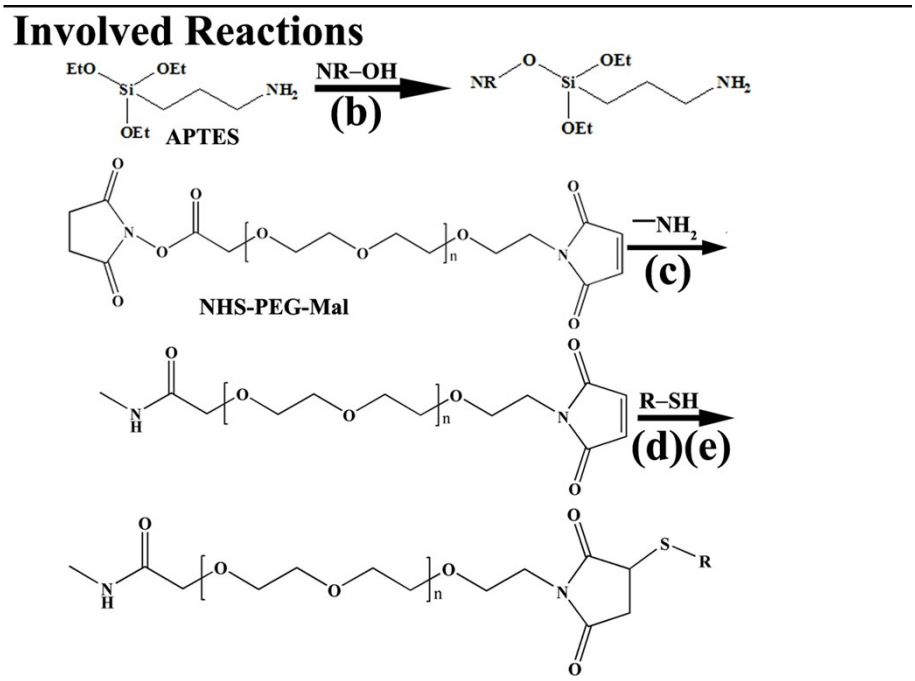

Scheme S1. The involved chemical reactions during the surface modification of Eu-Gd_2O_3 NRs. R-SH during reaction (d, e) represent HS-RGD and HS-CTX, respectively.

2. Results and Discussion

2.1. Phase analysis and morphology observation

To obtain crystallized and well-dispersed Eu-Gd_2O_3 NRs, the as-prepared Eu-$Gd(OH)_3$ NRs were calcined at different temperature (400 and 600 ^oC) for different time (4, 6, and 8 h) without any gaseous protection. XRD results (Fig. S1a) showed that all the obtained samples were cubic phase of Gd_2O_3 (ICDD 86-2477)[2]. SEM images (Fig. S1b ~ S1g) showed that the morphology of the samples varied with the calcination conditions, and the samples remained rod shape when calcined at 400 ^oC within 6 h (Fig. S1b, S1c), while they were changed to shorter and thicker NRs, some of which were merged together gradually at the calcination of 600 ^oC (Fig. S1e ~ S1g). Obviously, the sample in Fig. S1d displayed stubbed NRs for little merging with each other. Furthermore, the crystallinity of the samples calculated from Fig. S1a *via* Jade software was increased with the calcination temperature and time, while the average length decreased (Tab. S1). Higher crystallinity, finer size and better dispersibility could bring more significant positive bio-effects, such as the relaxivity of T_1-enhanced Magnetic Resonance (MR) imaging[3, 4]. Based on these results, the calcination at 400 ^oC for 8 h was considered as the optimal condition to obtain Eu-Gd_2O_3 NRs in this study.

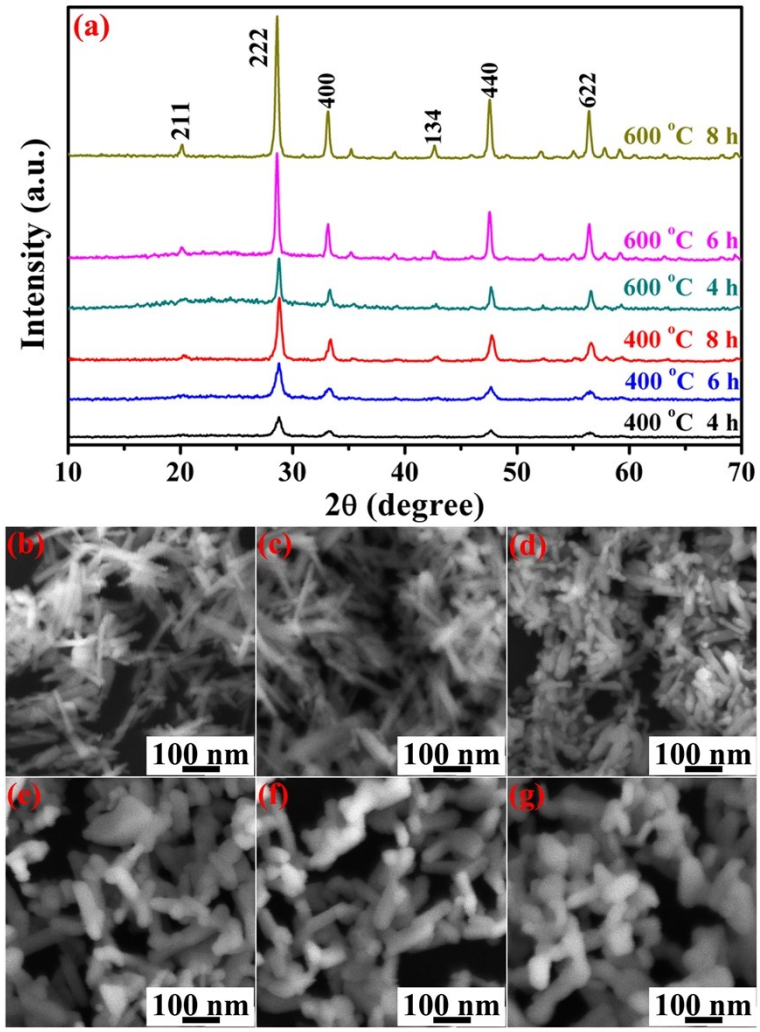

Fig. S1. (a) XRD patterns and (b ~ g) SEM images of the obtained Eu-Gd_2O_3 NRs from different calcination temperature and time: (b) 400 °C 4 h, (c) 400 °C 6 h, (d) 400 °C 8 h, (e) 600 °C 4 h, (f) 600 °C 6 h and (g) 600 °C 8 h.

Tab. S1. The crystallinity and average length of the Eu-Gd_2O_3 NRs samples obtained under different calcination conditions.

Calcination	**400 °C**			**600 °C**		
condition	**4 h**	**6 h**	**8 h**	**4 h**	**6 h**	**8 h**
Crystallinity (%)	70.31	79.29	89.61	75.88	84.59	91.79
Average length (nm)	180 ± 25	115 ± 17	78 ± 22	65 ± 11	60 ± 20	63 ± 25

2.2. Size Statistics

SEM image in Fig. S2a and S2b showed that the Eu-Gd_2O_3 products were rod-like, and the length distributions in Fig. S2c and S2d showed the average length of 200 ± 38 nm for the Eu-$Gd(OH)_3$ NRs precursors and 78 ± 22 nm for Eu-Gd_2O_3 NRs products, respectively, indicating that calcination could obtain the shorter NRs. As reported[3], smaller nanomaterials possessed larger surface-to-volume ratio, and more surface Gd ions in the surface could lead to their higher relaxivity. So, the obtained Eu-Gd_2O_3 NRs should be superior to the Eu-$Gd(OH)_3$ NRs precursors to be used as positive enhanced MR imaging contrast agents.

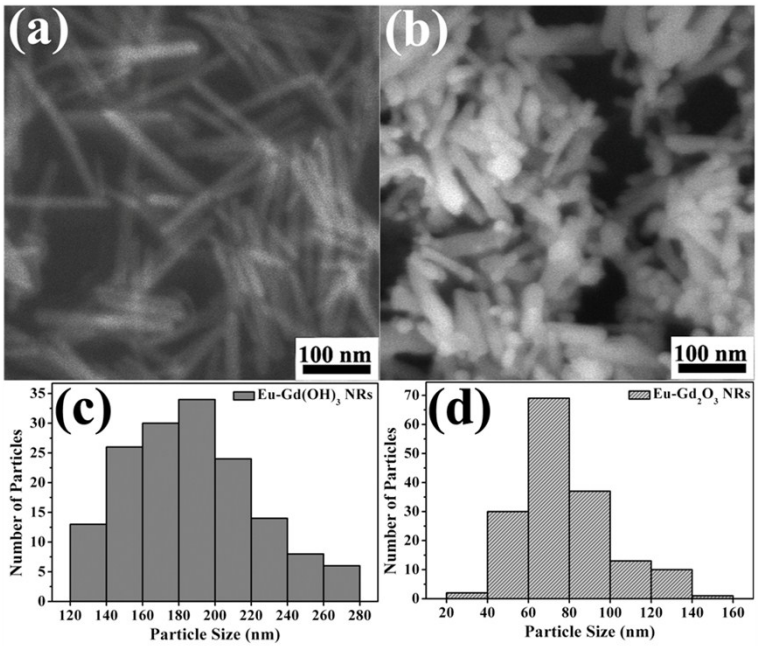

Fig. S2. SEM images of the obtained (a) Eu-$Gd(OH)_3$ precursors and (b) Eu-Gd_2O_3 products and (c, d) their length distributions, respectively. Each was obtained from over 200 objects based on SEM images.

2.3. Zeta-Potential Analysis and Ninhydrin Reaction

The prepared Eu-Gd_2O_3 NRs were treated in 7.0 wt.% TMAOH (tetramethyl ammonium hydroxide) aqueous solution to obtain abundant –OH groups on their surface. However, the reaction temperature would obviously affect the degree of hydroxylation. As reported[5], the number of –OH groups on the NRs surface could influence their surface charge, which could be measured by zeta-potential. In Fig. S3a, the negative zeta-potential of the hydroxylated NRs was increased with the reaction temperature, indicating that the number of –OH groups on the NRs surfaces was increased with the reaction temperature. In details, compared with the untreated group, the zeta-potential values of the NRs treated under 80 ^oC were not increased obviously, while those of the NRs treated at more than 80 ^oC were increased significantly ($p < 0.05$). Especially, the zeta-potential value of the NRs treated at 180 ^oC was significantly higher than that of the NRs treated at 80 ^oC.

The hydroxylated Eu-Gd_2O_3 NRs were aminated with APTES (3-aminopropyl-triethoxysilane) solution to acquire sufficient –NH_2 on their surface. Similarly, the zeta-potential values of the aminated Eu-Gd_2O_3 NRs in different reaction temperature were showed in Fig. S3b, suggesting the best effect of amination at 70 ^oC, significantly higher than the control group (hydroxylated Eu-Gd_2O_3 NRs, $p < 0.05$). The photograph of the reactive liquid of the aminated Eu-Gd_2O_3 NRs with ninhydrin solution (Fig. S3c) showed the darkest purple color at 70 ^oC, and the UV absorption of their supernatant (Fig. S3d) demonstrated the highest absorption at about 400 nm, indicating the biggest concentration of ruhemann's purple, resulting from the reaction products of ninhydrin and the largest amounts of –NH_2 groups on the surface of aminated Eu-Gd_2O_3 NRs.

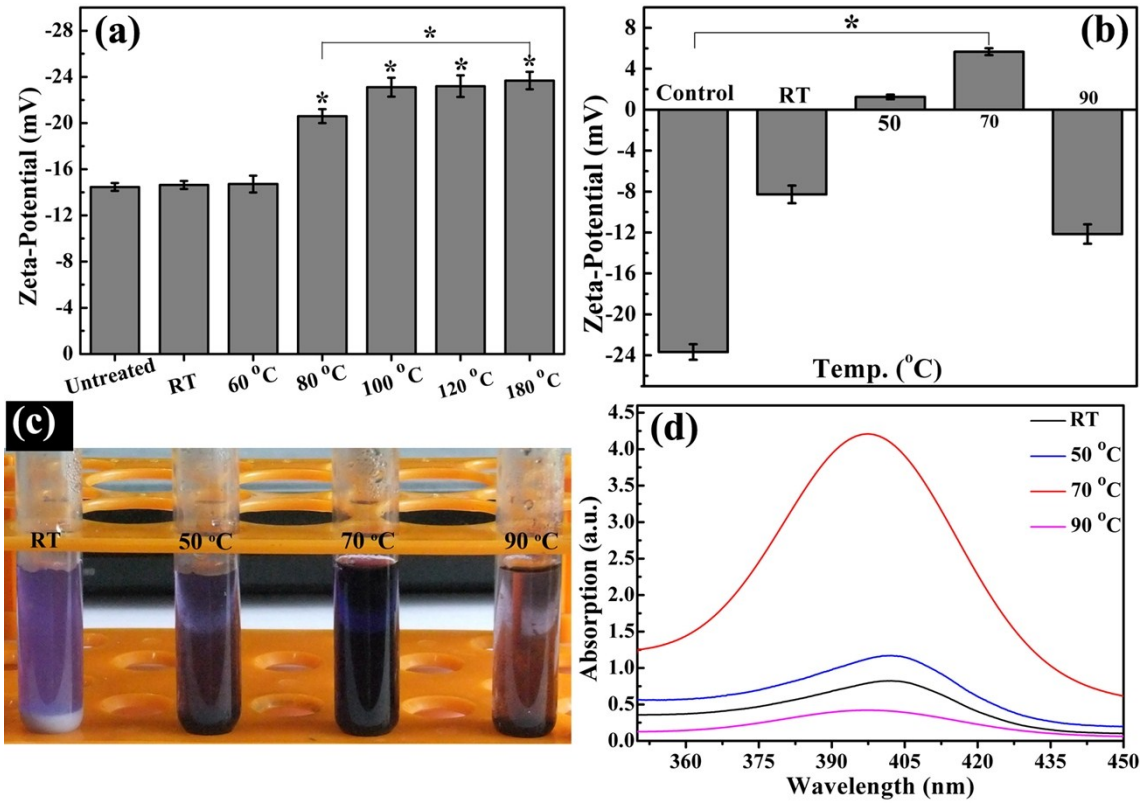

Fig. S3. Zeta-potential values of (a) hydroxylated Eu-Gd_2O_3 NRs, (b) aminated Eu-Gd_2O_3 NRs obtained from different reaction condition, and these NRs were dispersed in PBS solution at pH = 7.4; (c) the photograph of reaction liquid of aminated Eu-Gd_2O_3 NRs with ninhydrin in deionized water at different reaction temperature; (d) UV absorption of their supernatant; *$p < 0.05$ represents the significant difference with the untreated group and the corresponding groups.

2.4. Elements analysis

XPS spectra in Fig. S4a showed that the prepared pure NRs were consisted of Gd, Eu and O elements, implying that Eu ions were doped into gadolinium oxides samples. After a series of surface treatment and modified with PEG molecule and RGD peptides, there were Cl, C, N, Si, S elements in RGD-NRs (red line in Fig. S4a), which were introduced by CCl_4 reagent during the amination, PEGylation and RGD modification, respectively. Furthermore, the existence of Si (from APTES during amination), N and S elements in RGD-NRs indicated the sufficient PEGylation of PEG-NRs, and successful conjugation of RGD on the RGD-NRs surface. The elements contents of pure NRs and RGD-NRs in Tab. S2, showed that Eu/Gd ratio of pure NRs and RGD-NRs was 0.245/1, near to the ratio of raw regents (0.25/1). 3d XPS spectrum of Eu in pure NRs (Fig. S4b) demonstrated the existence of $Eu^{2+}{}_{3d\ 5/2}$ and $Eu^{3+}{}_{3d\ 5/2}$, which could lead to great contribution to redox responsive MR imaging[6]. Moreover, the peak at 164.1 eV in the 2p XPS spectrum of S (Fig. S4c), well corresponding with the binding energy of C–S bond[7], further demonstrated the well conjugation of HS-RGD with NRs.

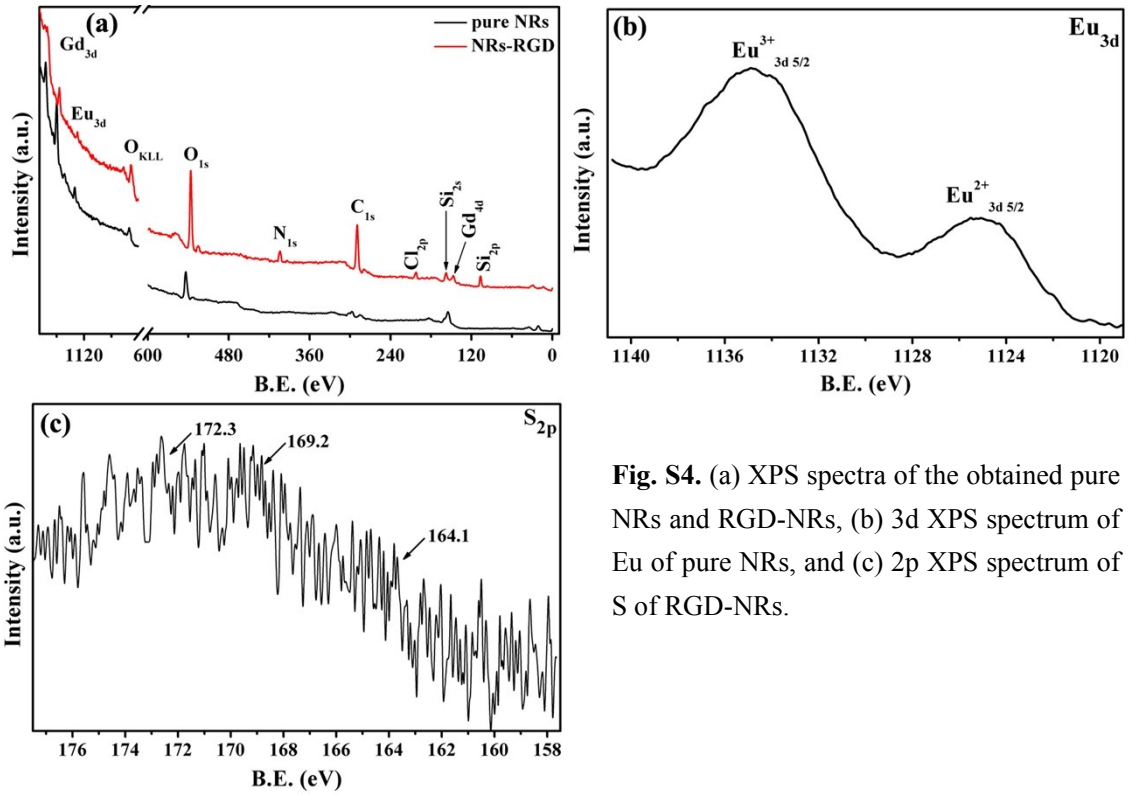

Fig. S4. (a) XPS spectra of the obtained pure NRs and RGD-NRs, (b) 3d XPS spectrum of Eu of pure NRs, and (c) 2p XPS spectrum of S of RGD-NRs.

Tab. S2. Elements contents of the obtained pure NRs and RGD-NRs (at.%)

Elements	Gd	Eu	O	N	C	Cl	Si	S	Eu/Gd
pure NRs	45.98	11.28	42.74						0.245/1
RGD-NRs	7.26	1.78	43.27	9.71	20.4	3.49	14.06	< 1	0.245/1

2.5. Luminescent property

Fig. S5 is the fluorescence excitation and emission spectra of the as-prepared Eu-Gd_2O_3 NRs. the peak at 506 nm in Fig. S5b is mainly ascribed to the $^5D_1 \rightarrow {}^7F_0$ transition of Gd ions and part ascribed to the electron-dipole allowed 4*f*–5*d* transition of Eu^{2+} ions, and the peak at 611 nm is corresponding to $^5D_0 \rightarrow {}^7F_2$ electron transitions in Eu^{3+}, due to efficient energy from Gd^{3+} to Eu^{3+} when the Eu-Gd_2O_3 NRs were excited at 393 nm[8]. Photograph inset in Fig. S5b shows very strong pink luminescence of Eu-Gd_2O_3 NRs dispersed in PBS solution excited at 405 nm, indicating that Eu-Gd_2O_3 NRs have the potential applications in bioprobe fields.

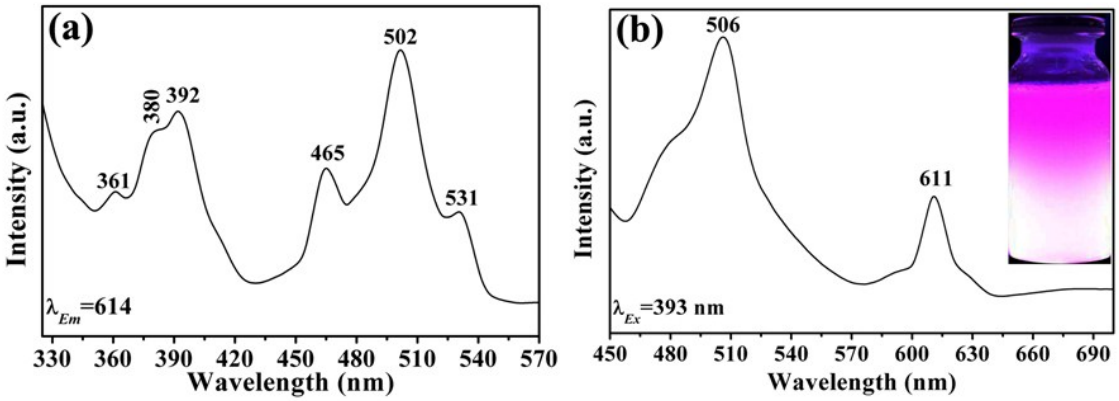

Fig. S5. (a) Excitation and (b) emission spectra of Eu-Gd_2O_3 NRs, and the inset was a photograph of Eu-Gd_2O_3 NRs-dispersed PBS (1 mg/mL) under UV light of 405 nm wavelength.

2.6. Cell observation & cytotoxicity assay

As reported[9-11], PEG molecule linkage could prominently improve the biocompatibility of materials, so it is necessary to evaluate the cytotoxicity of the obtained pure NRs and PEG-NRs. After cells were co-cultured with different concentrations of pure NRs or PEG-NRs for 2 d, the morphology of L929 cells, HUVECs and U251 cells were observed and shown in Fig. S6. In Fig. S6, L929 cells without NRs grew well, and some cells were touching the NRs (marked by green arrows in Fig. S6). L929 cells remained normal cellular morphology with obvious pseudopods (marked by black arrows in Fig. S6) when treated by pure NRs of not more than 50 $\mu g \cdot mL^{-1}$, but some cells changed round and lost pseudopods (marked by yellow arrows in Fig. S6) when treated by pure NRs of more than 100 $\mu g \cdot mL^{-1}$, indicating the cytotoxicity of pure NRs in higher concentrations. However, L929 cells with normal cellular morphology grew well when treated by PEG-NRs even of 100 $\mu g \cdot mL^{-1}$, demonstrating that the lower cytotoxicity of PEG-NRs due to PEG molecule linkage. Then, the results of the co-incubation of pure NRs or PEG-NRs with HUVECs and U251 cells were similar to those on L929 cells, further indicating that PEG coating improved the cytocompatibility of the obtained NRs.

Further quantitation of cell viability under the treatment of pure NRs and NRs-PEG was performed by MTT tests. The results in Fig. S7 showed that the cell viabilities were significantly inhibited when the concentrations of pure NRs were more than 100 $\mu g \cdot mL^{-1}$ ($p < 0.01$) for L929 cells, more than 50 $\mu g \cdot mL^{-1}$ ($p < 0.05$) for HUVECs, and more than 25 $\mu g \cdot mL^{-1}$ ($p < 0.01$) for U251 cells, respectively, however, the cell viabilities were significantly promoted when the concentrations of PEG-NRs were less than 25 $\mu g \cdot mL^{-1}$ for L929 cells ($p < 0.05$). Furthermore, cell viabilities of HUVECs and U251 cells were not obviously inhibited when the treated concentrations of PEG-NRs were 200 $\mu g \cdot mL^{-1}$ or 50 $\mu g \cdot mL^{-1}$. These results demonstrated that PEG-NRs had little cytotoxicity, and obviously lower than that of pure NRs.

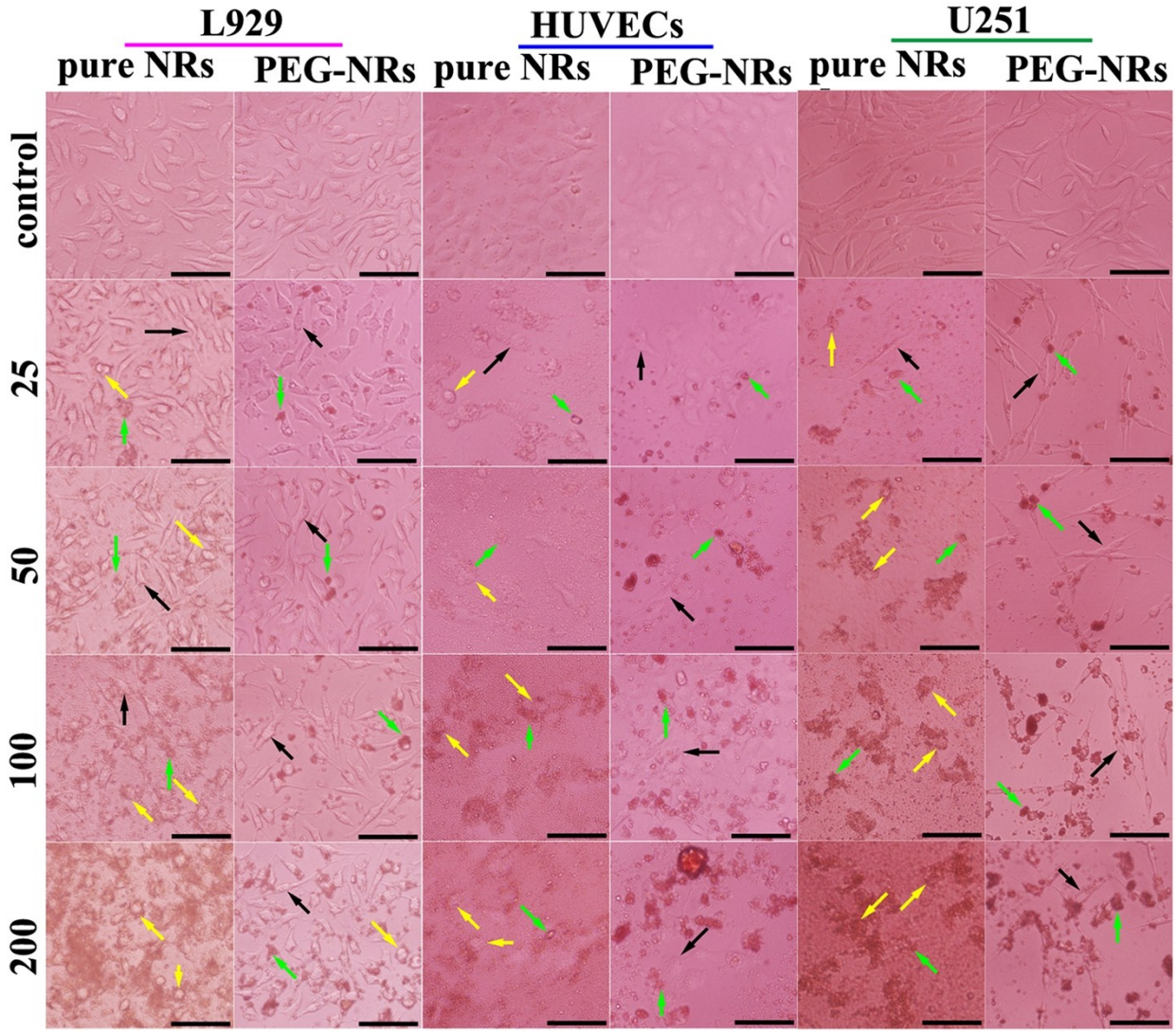

Fig. S6. The photographs of L929, HUVECs and U251 cells treated with different concentrations of pure Eu-Gd_2O_3 NRs or PEG-NRs for 2 d, respectively. The unit was $\mu g \cdot mL^{-1}$. Black, yellow and green arrows showed cells with normal morphologies, abnormal morphologies and the co-cultured NRs, respectively. Scale bars: 100 μm.

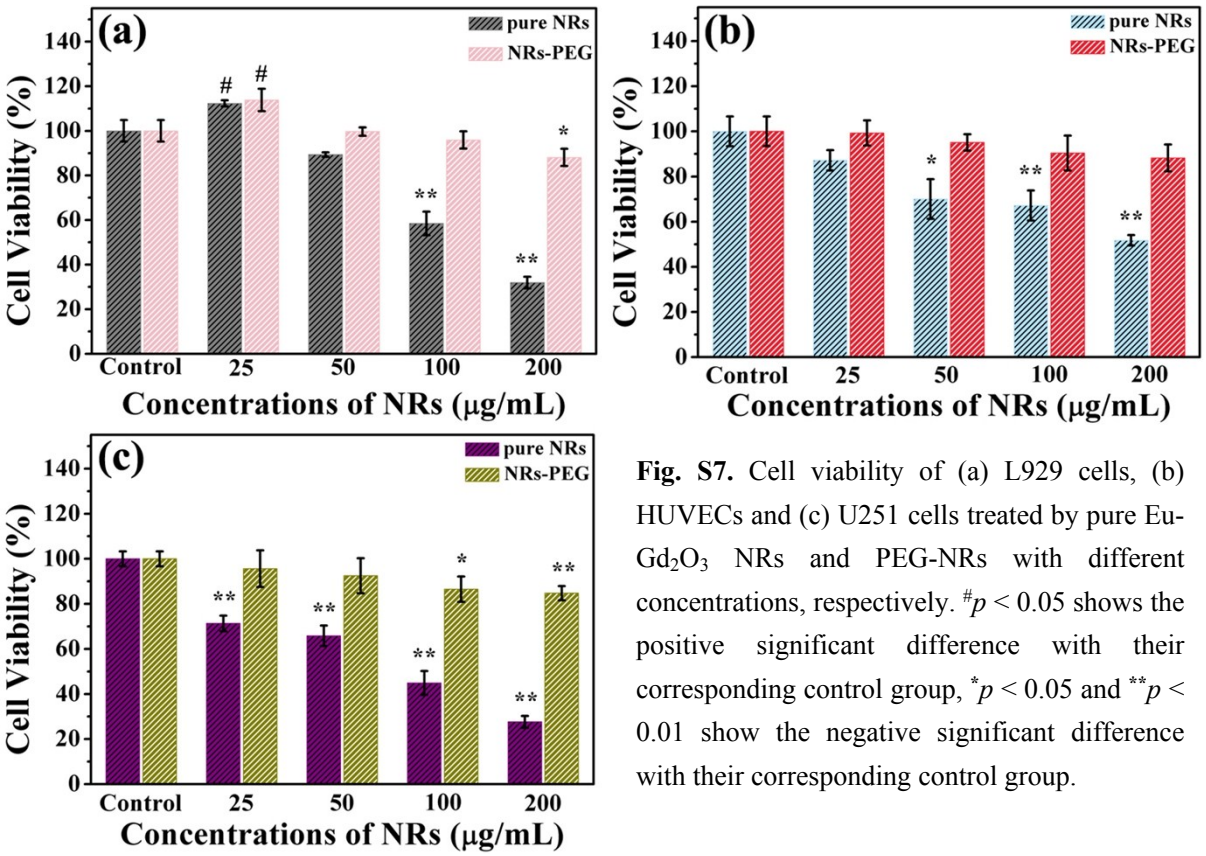

Fig. S7. Cell viability of (a) L929 cells, (b) HUVECs and (c) U251 cells treated by pure Eu-Gd_2O_3 NRs and PEG-NRs with different concentrations, respectively. $^{\#}p < 0.05$ shows the positive significant difference with their corresponding control group, $^{*}p < 0.05$ and $^{**}p < 0.01$ show the negative significant difference with their corresponding control group.

2.7. Targeting images

Fig. S8 is the photographs of the HUVECs and U251 cells co-cultured with Eu-Gd_2O_3 NRs for 24 h at a concentration of 200 $\mu g \cdot mL^{-1}$, and it is observed that NRs were adhered on cell membranes (shown by red arrows). PEG-NRs in Fig. S8 were hardly captured by cells, and some PEG-NRs were adhered on cell membrane, indicating the no targeting property of PEG-NRs for HUVECs and U251 cells. However, RGD-NRs showed more adherences on cell membrane, owing to the high affinity of RGD with laminin of HUVECs and U251 cells. Interestingly, CTX-NRs were hardly captured by HUVECs, but largely adhered on the cell membrane of U251 cells, revealing the specific targeting property of CTX for U251 cells, owing to the specific binding of CTX with MMP-2, which was only highly-expressed on the cell membrane of U251. Moreover, U251 cells presented round, and growth density of U251 decreased obviously, suggesting the limitation effect of CTX to U251 cells. Finally, RGD-NRs-CTX were massively captured by HUVECs and U251 cells, because of the affinity effect of RGD on laminin of cell surfaces, and the specific targeting behavior of CTX with U251 cells.

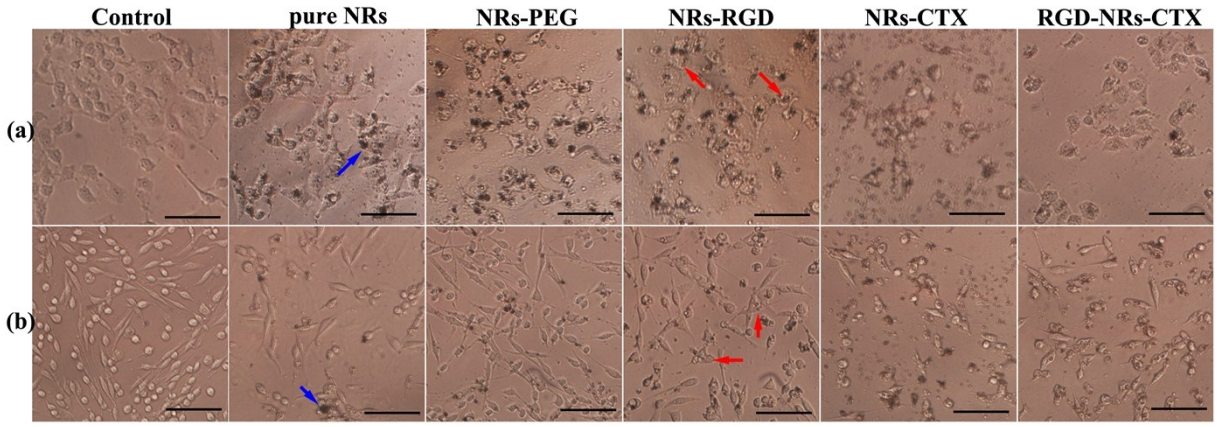

Fig. S8. The photographs of (a) HUVEC and (b) U251 cells co-cultured with different NRs at a concentration of 200 $\mu g \cdot mL^{-1}$ for 24 h. Blue and red arrows showed the agglomerates and well-dispersed NRs adhered to living cells, respectively. Scale bars: 100 μm.

2.8. Inhibitory effect of Eu-Gd_2O_3 NRs

After U251 cells were co-incubated for 2 d with RGD-NRs, CTX-NRs and RGD-NRs-CTX at different concentrations (Fig. S9), the shape and density of U251 cells presented obvious difference. In the control group, U251 cells grew well with normal cellular morphology and moderate growth density. After treated with RGD-NRs with the concentrations of lower than 125 $\mu g \cdot mL^{-1}$, U251 cells showed normal morphology and growth density, and were slightly affected on growth density at the NRs concentration of 1000 $\mu g \cdot mL^{-1}$, indicating the slightly inhibitory effect of RGD-NRs on U251 cells. However, the morphology and growth density of U251 cells were seriously affected after they were treated with 62.5 $\mu g \cdot mL^{-1}$ of CTX-NRs or RGD-NRs-CTX, resulting from the efficient inhibition ability of CTX on U251 cells. Furthermore, the cellular influence caused by RGD-NRs-CTX was more obvious than that caused by CTX-NRs, indicating the superimposed effect of RGD and CTX in the inhibition of U251 cells. These results demonstrated that the as-prepared RGD-NRs-CTX could be potentially used as therapeutic agents for U251 tumors *in vivo*.

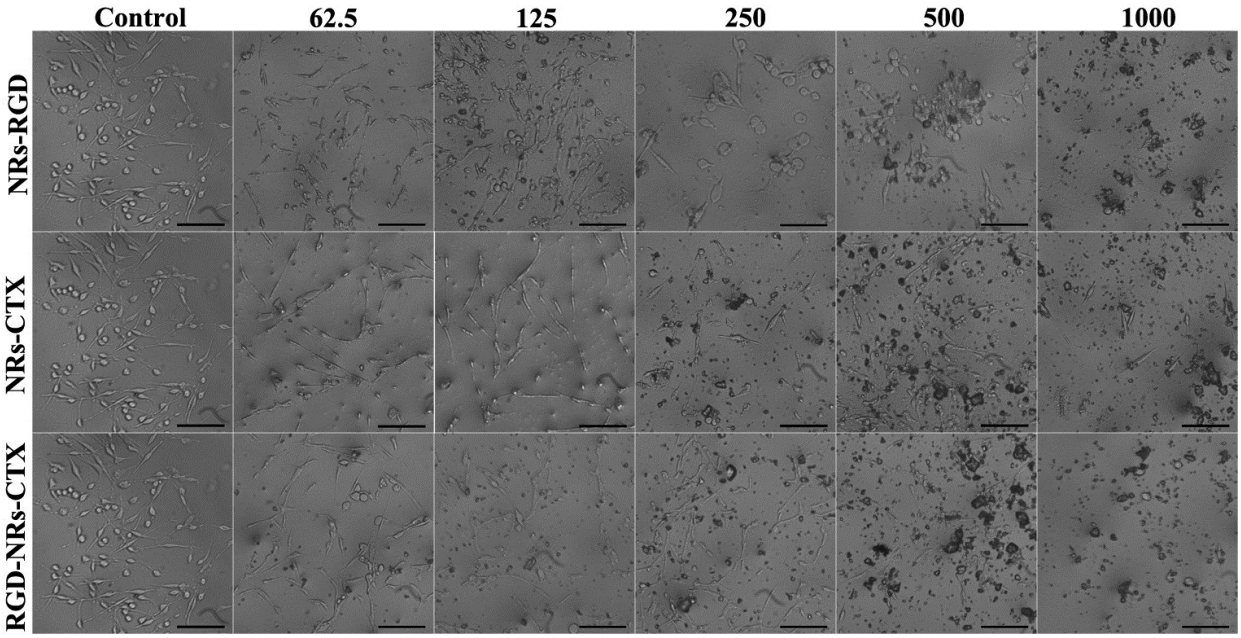

Fig. S9. Photographs of U251 cells after treated with different concentrations of RGD-NRs, NRs-CTX and RGD-NRs-CTX NRs for 2 d, respectively. The unit was $\mu g \cdot mL^{-1}$, scale bars: 100 μm.

2.9. Cell cycle analysis

Herein, L929 cell was used as a non-cancer cell model and the cell cycle was measured after co-cultured for 24 h with 100 $\mu g \cdot mL^{-1}$ of pure NRs, PEG-NRs, RGD-NRs, CTX-NRs and RGD-NRs-CTX, respectively, to analyze the influence of these NRs on normal cells. As shown in Fig. S10b ~ S10f, the phase distribution of L929 cycle was similar with each other, slightly different from that of the control in Fig. S10a, suggesting that these NRs have little influence on the cycle of L929 cell, especially PEG, RGD and CTX did not produce significant difference on the cell cycle. Moreover, the percentages within each phase of L929 cell cycle were shown in Fig. S10g. Compared with the control, the percentages in dead phase of each test group increased at same level, and those in G2-M phase decreased similarly, resulting from the cytotoxicity of Eu-Gd_2O_3 NRs, indicating that CTX-modified Eu-Gd_2O_3 NRs showed no specific ability to kill normal cells.

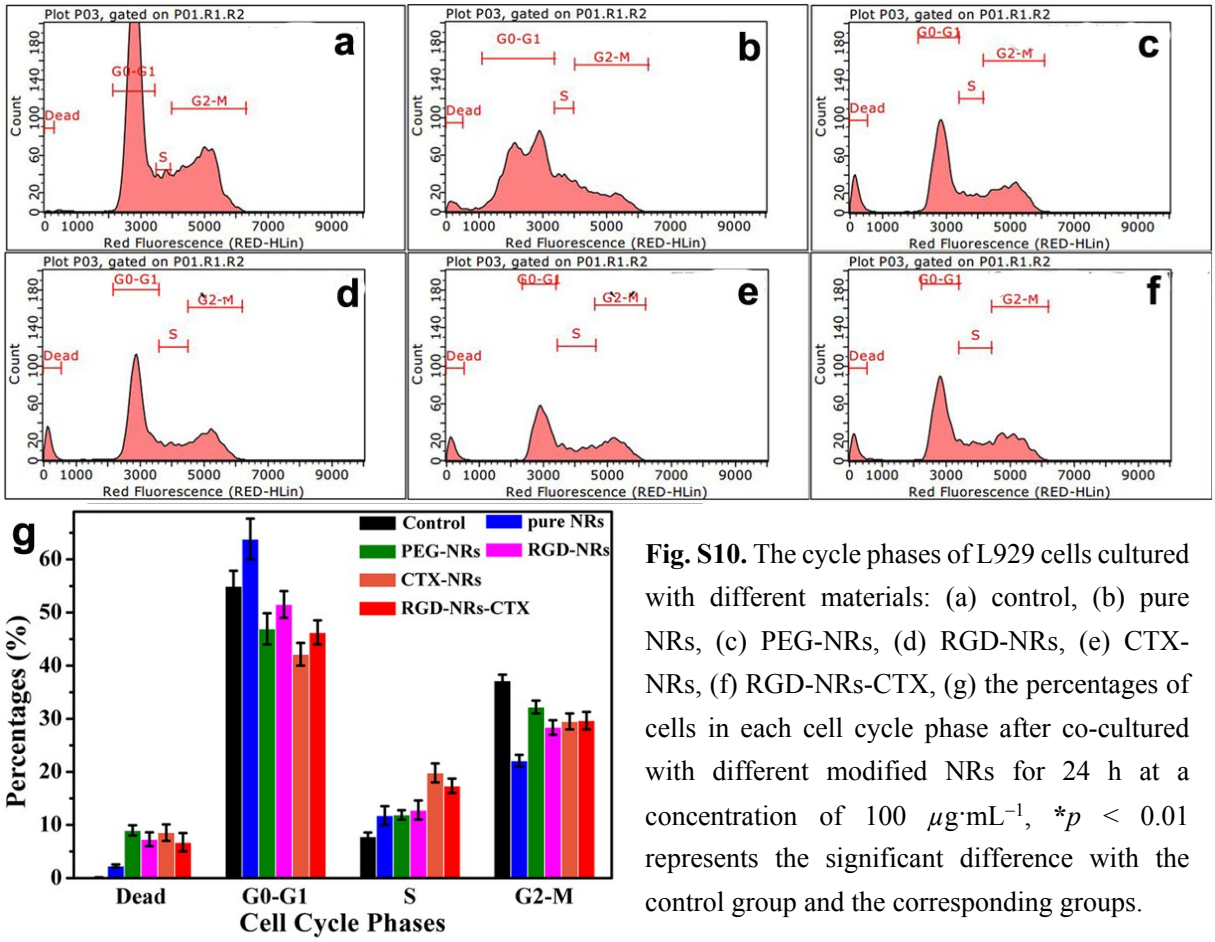

Fig. S10. The cycle phases of L929 cells cultured with different materials: (a) control, (b) pure NRs, (c) PEG-NRs, (d) RGD-NRs, (e) CTX-NRs, (f) RGD-NRs-CTX, (g) the percentages of cells in each cell cycle phase after co-cultured with different modified NRs for 24 h at a concentration of 100 $\mu g \cdot mL^{-1}$, $*p < 0.01$ represents the significant difference with the control group and the corresponding groups.

2.10. Hemolysis

Hemolysis may lead to organ failure and patient death during blood transfusion [12], which represents the rupture of red blood cell (RBC) with the direct release of hemoglobin (Hb) into the suspending medium, and hemolysis assay *in vitro* was usually taken to evaluate the interaction between nanomaterials and blood components [13, 14]. Fig. S11a showed that the hemolysis ratio of PEG-NRs was far lower than that of pure NRs at each concentration, owing to the biocompatible PEG coating layer. Noticeably, the hemolysis ratio of PEG-NRs only reached to 4% at a high concentration of 2000 $\mu g \cdot mL^{-1}$, which was acceptable for the application of biomaterials *in vivo*. The inset photographic image in Fig. S11a displayed the the hemolysis results. The color of the supernate in PEG-NRs group was extremely light, showing no difference with that in the negative, while the pure NRs group was deep red and the color concentration-dependently increased, close to that in the positive at the concentration of 2000 $\mu g \cdot mL^{-1}$, implying that there was little RBC broken in PEG-NRs group. The UV absorption around 541 and 580 nm in Fig. S11b may further semi quantify the amount of Hb in the supernate, indicating the extremely low hemolysis of PEG-NRs and the feasibility for further application *in vivo*.

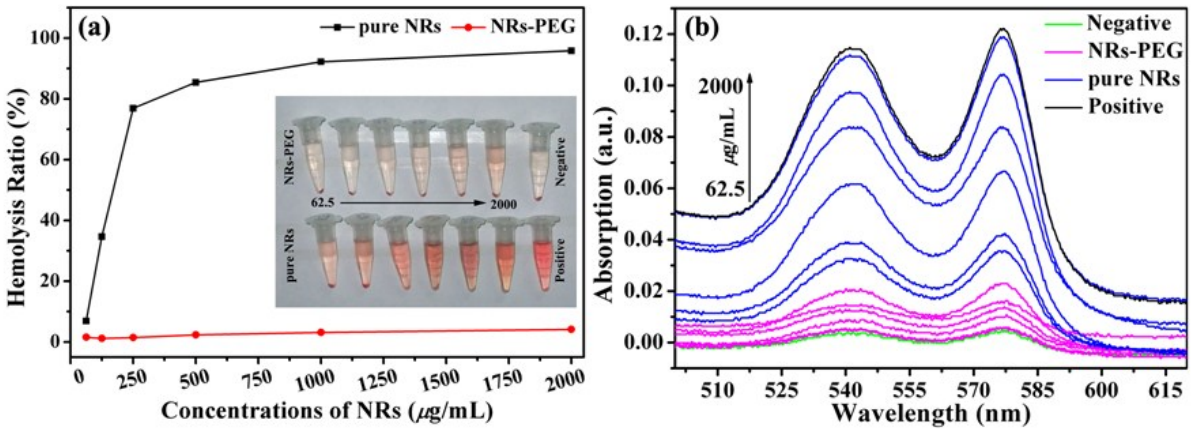

Fig. S11. (a) The concentration-dependent hemolysis ratio of pure NRs and PEG-NRs, and (b) the UV-vis absorption spectra to detect the hemoglobin in the supernatant after interacted with NRs, an inset in (a) was their photographic images for direct observation of hemolysis.

2.11. Toxicity *in vivo* & Bio-distribution

In order to investigate the long-term toxicity and *in vivo* biodistribution of the Eu-Gd_2O_3 NRs, the body weights of the tested rats were recorded, and organs were collected from the tested rats 1 or 10 d after the administration of Eu-Gd_2O_3 NRs *via* tail vein. In Fig. S12a, the body weights of all the Eu-Gd_2O_3 NRs-injected groups increased slightly in a pattern similar to that of the control group, and there was no significant difference between any test groups, indicating that the negligible toxicity of the Eu-Gd_2O_3 NRs at a dose of 10 mg Gd/kg rats for 10 d. Besides, there were no changes in eating, drinking, fur color, exploratory behavior, activity and neurological status of rats under the 10-day behavior observation for each group. To further determine whether these Eu-Gd_2O_3 NRs caused any harmful effect or disease, the main organs of the test SD rats 1 or 10 d after the administration of different Eu-Gd_2O_3 NRs (shown in Fig. S12b) were collected, and the Gd ion concentrations in each organ were analyzed. As shown in Fig. S12c, at 1 d of the NRs administration, the Gd ions concentrations in the liver, spleen, lung and faeces of the pure NRs-injected SD rats were significantly higher than those in other 4 groups ($p < 0.01$), resulting from the bad blood compatibility, short blood half-life time and poor dispersibility of the pure NRs, which could lead to their quick uptake by RES in liver and spleen, rapid filtration in lung, and high-speed elimination through faeces and urine, similar to the *in vivo* behavior of many other nanomaterials[15, 16]. However, the concentration of Gd ions in blood of the pure NRs-injected SD rat was prominent lower than that of the other 4 groups ($p < 0.01$). Moreover, because of the low amount of modified RGD and CTX, the biodistribution and circulation in blood of RGD-NRs, CTX-NRs and RGD-NRs-CTX showed no difference with that of the PEG-NRs. For long-term toxicity *in vivo*, the long retention time of Eu-Gd_2O_3 NRs in main organs were investigated. Fig. S12d showed that Gd ions in the main organs, blood and faeces were extremely low at 10 d of the NRs administration, indicating that Eu-Gd_2O_3 NRs were almost completely eliminated *via* the SD rats' metabolism. Histological assessment was introduced to research effects of the Eu-Gd_2O_3 NRs on the main organs. As illustrated in Fig. S13 and S14, no obvious tissue damages were observed on the H & E stained slices of heart, liver, spleen, lung and kidney extracted from the test SD rats treated for 1 or 10 d, suggesting that all the prepared Eu-Gd_2O_3 NRs presented very low toxicity

or nontoxicity in SD rats at treatment levels.

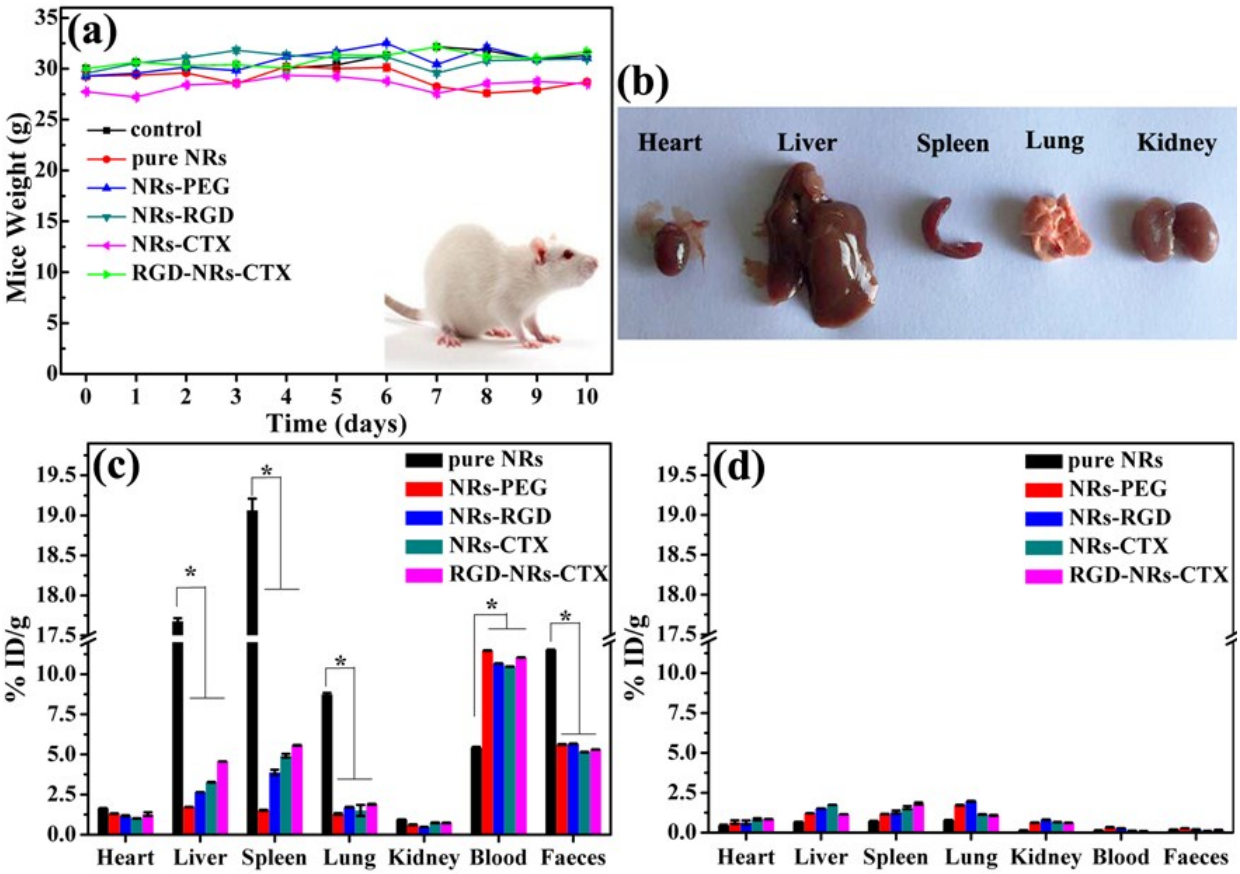

Fig. S12. (a) The line chart of the change in SD rats' body weight (n = 5), (b) photographs of the heart, liver, spleen, lung and kidney extracted from the tested SD rats, and (c, d) the bio-distribution of the Gd ions in SD rats' organs, blood and faeces after the treatment with Eu-Gd_2O_3 for (c) 1 d and (d) 10 d at 10 mg Gd/kg rats, respectively. Inset: the photograph of one SD rat used in this investigation. **p* <0.01 shows the significant difference between the corresponding groups.

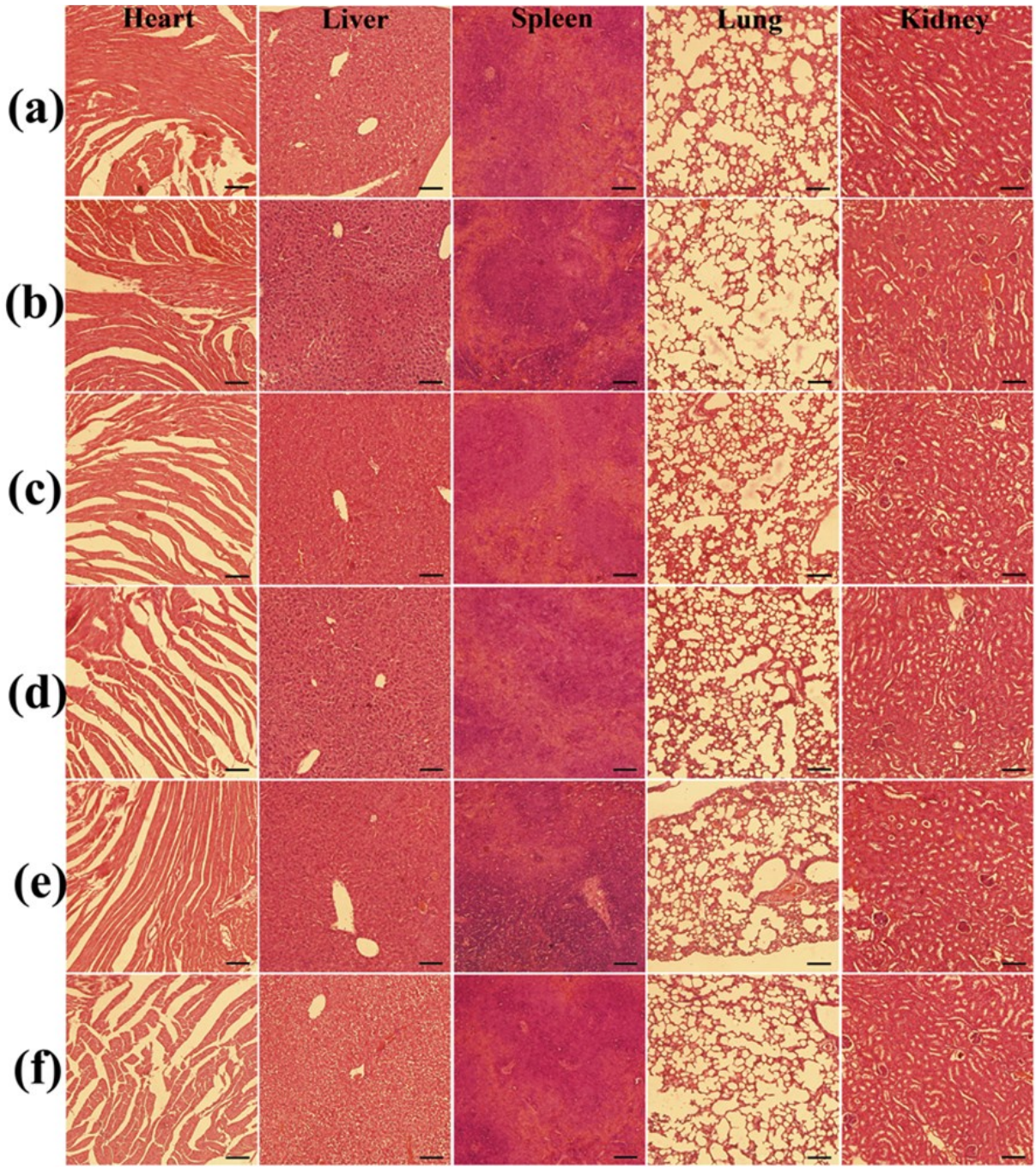

Fig. S13. H & E-stained slices of heart, liver, spleen, lung and kidney extracted from SD rats after administrated with different Eu-Gd_2O_3 NRs at a concentration of 10 mg Gd/kg rats for 1 d, (a) control group (no NRs), (b) pure NRs, (c) PEG-NRs, (d) RGD-NRs, (e) CTX-NRs and (f) RGD-NRS-CTX, respectively. Scale bars: 100 μm.

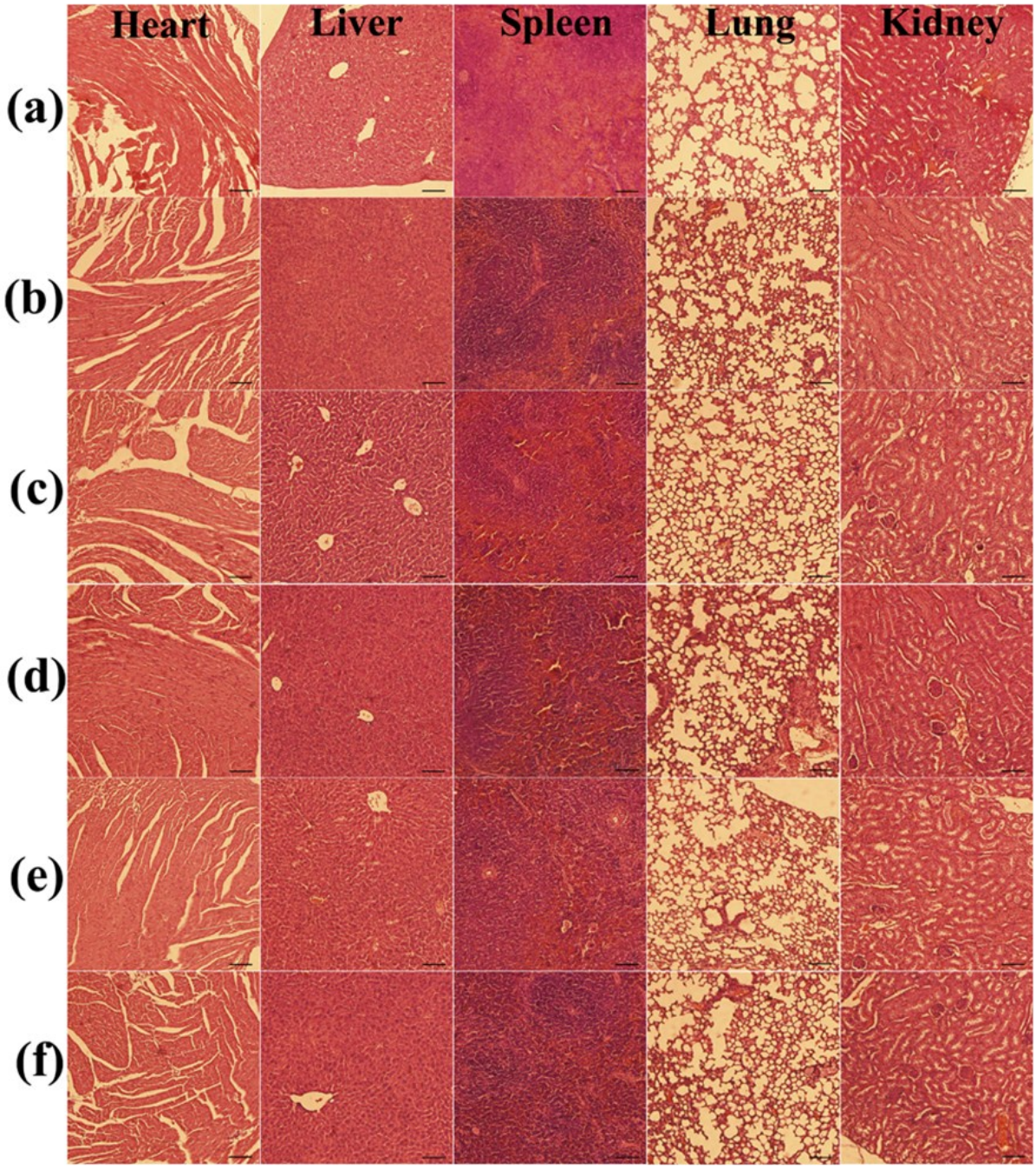

Fig. S14. H & E-stained slices of heart, liver, spleen, lung and kidney extracted from SD rats after administrated with different Eu-Gd_2O_3 NRs at a concentration of 10 mg Gd/kg rats for 10 d, (a) control group (no NRs), (b) pure NRs, (c) PEG-NRs, (d) RGD-NRs, (e) CTX-NRs and (f) RGD-NRS-CTX, respectively. Scale bars: 100 μm.

2.12. MR imaging *in vivo*

MR imaging was used *in vivo* to evaluate the enhancement property of the obtained Eu-Gd_2O_3 NRs. A series of T_1-weighted MR images in the tumor regions of the TBN mice acquired pre-/post-injection of pure NRs, RGD-NRs and RGD-NRs-CTX were shown in Fig. S15. Three MR images of tumor regions before the injection of pure NRs, RGD-NRs and RGD-NRs-CTX exhibited hypo-intensity and obscure tumor boundary, and three typical images of the corresponding tumor regions of 3 and 24 h of post-injection of pure NRs in sequence hardly displayed changes on the brightness and tumor boundary, resulting from the bad blood affinity and dispersibility, no targeting ability to tumor and no accumulative property in tumor regions. On the contrary, six images of the corresponding tumor regions with 3 and 24 h of post-injection of RGD-NRs and RGD-NRs-CTX in sequence revealed the increased signal and clearer tumor boundary, owing to their good affinity and dispersibility in blood, high relaxivity, considerable adhesive capacity with laminin of RGD to cause accumulation, and special targeting ability of CTX to tumor. Especially, the increase in the contrast intensity between tumor interior and periphery of RGD-NRs-CTX-injected TBN mice was significantly higher than that of the RGD-NRs-injected TBN mice at 3 and 24 h of the post-injection, respectively, indicating that the synergistic effect of RGD and CTX was better than single RGD effect and the prepared RGD-NRs-CTX showed preferable potential application in MR imaging as targeting contrast agents.

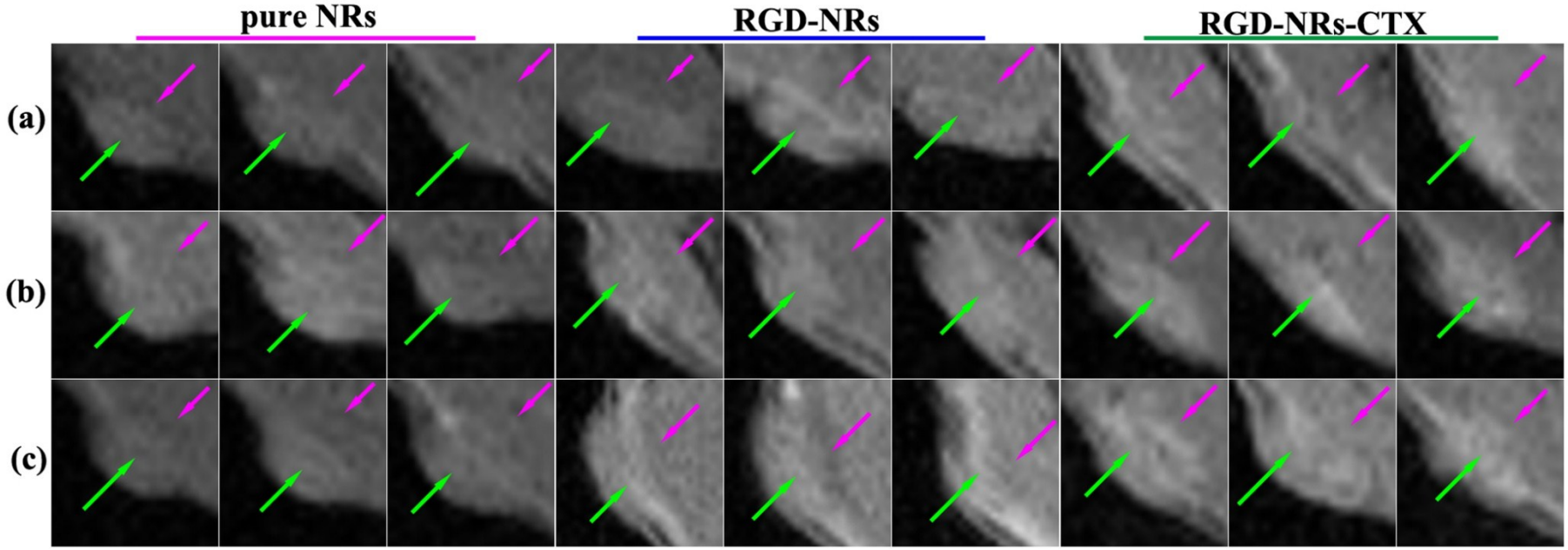

Fig. S15. MR images of the TBN mice at tumor site and periphery after the administration of pure NRs, RGD-NRs and RGD-NRs-CTX, (a) 0 h (pre-injection), (b) 3 h and (c) 24 h of post-injection, respectively. Green arrows showed the tumor interior and pink arrows showed the tumor periphery.

2.13. Cellular luminescence imaging

Fig. S16 showed the cellular luminescence imaging of pure NRs, PEG-NRs, RGD-NRs and CTX-NRs. In the dark field with UV excitation, DAPI-labeled cell nucleus displayed the number and position of the co-cultured U251 cells. In the bright field, the position and shape of U251 cells could be observed clearly. However, when excited by green light in dark field, the NRs adhered on cell membrane and internalized by U251 cells exhibited pink luminescence with different intensity. Compared with pure NRs and PEG-NRs groups, RGD-NRs and CTX-NRs groups showed more noticeable red luminescence, which could clearly delineate the cell shapes, and well coincide with the position and shape displayed by bright field and DAPI-labeled nucleus, due to the higher accumulation of NRs adhered on U251 cells membrane by the good targeting and adherence properties of RGD and CTX.

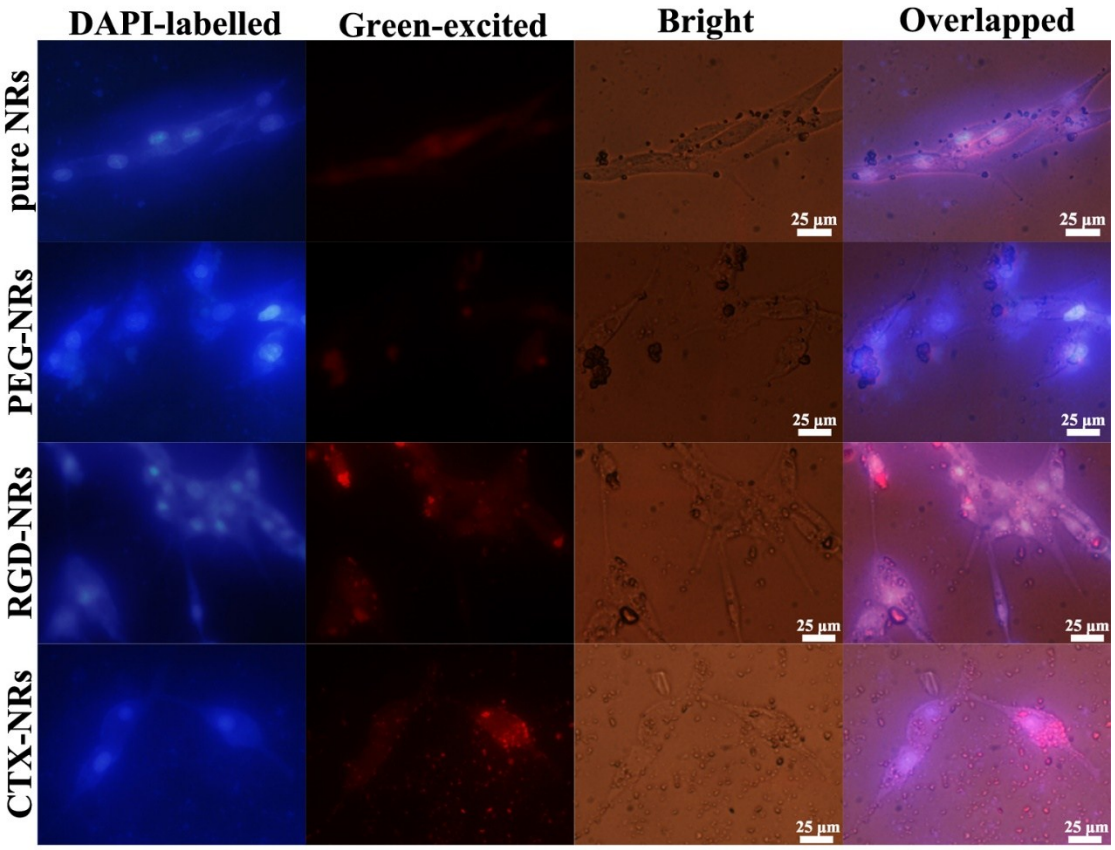

Fig. S16. The luminescence images of U251 cells co-cultured with 25 $\mu g \cdot mL^{-1}$ pure Eu-Gd_2O_3 NRs, PEG-NRs, RGD-NRs and CTX-NRs for 12 h.

2.14. Luminescence imaging *in vivo*

The luminescence imaging of PEG-NRs *in vivo* was further performed on TBN mice. The result in Fig. S17 showed that the injected PEG-NRs exhibited weaker luminescence signal in dark field under blue light excitation, due to their bad filtration property in U251 tumor.

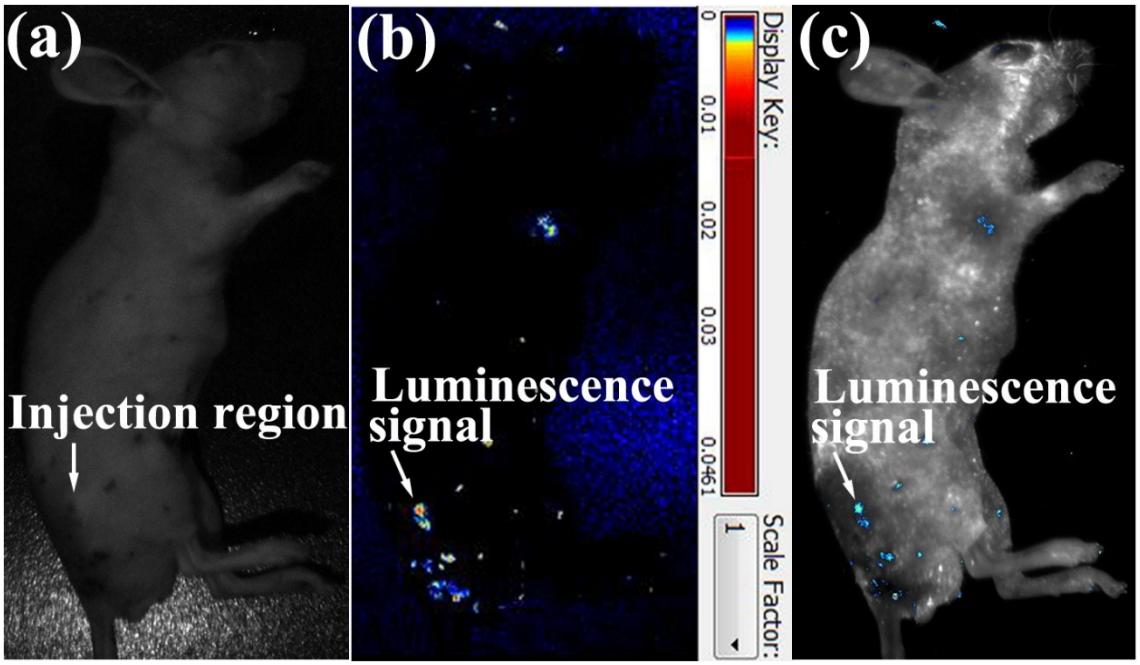

Fig. S17. *In vivo* luminescence imaging of TBN mice after injected with PEG-NRs: (a) white light, (b) blue light and (c) overlapped images.

2.15. Tumor limitation investigation

TBN mice were administrated with physiological saline solution, pure NRs, RGD-NRs and RGD-NRs-CTX *via* tail vein, and photographed each 5 d in the whole process. As shown in 1st ~ 5th of Fig. S18, the tumor sizes of the control group (in physiological saline solution-injected mice) were increased with time, and the tumor sizes of pure NRs-injected and RGD-NRs-injected TBN mice were increased in a similar range, indicating the no therapy effect of pure NRs and RGD-NRs for U251 tumor. Whereas, the tumor size of the RGD-NRs-CTX-injected TBN mice hardly changed and approximated to the initial size, demonstrating that RGD-NRs-CTX could effectively inhibit the U251 tumor the growth.

Furthermore, the H & E stained slices of heart, liver, spleen, lung and kidney extracted from the tested TBN mice were observed. As shown in Fig. S19, the shapes of all organs from the RGD-NRs-CTX-injected TBN mice were normal, and these organs were hardly different from those of the control group. In details, cardiac muscle tissue in the heart showed no hydropic degeneration, hepatocytes in the liver reflected no inflammatory infiltrates, perfect spleen sinus morphology in spleen indicated no tissue inflammatory, pulmonary alveoli in the lung samples appeared no pulmonary fibrosis, and the clear glomerulus structures in kidney revealed no renal damage. No necrosis was found in all organs from the RGD-NRs-CTX-injected TBN mice. These results demonstrated that RGD-NRs-CTX showed nontoxicity on normal organs and tissues in the whole process of tumor therapy. However, there was obvious hyperplasia in the periarteriolar lymphoid sheath (PALS) of the white pulp (pointed by black arrows) of the pure NRs-injected and RGD-NRs-injected TBN mice, respectively, which was also observed in other nanoparticles-treated spleen tissue[17, 18]. Moreover, serious pulmonary fibrosis was observed in the lung of pure NRs-injected TBN mice (shown by green circle), and severe glomerulus inflammatory was found in the kidneys of pure NRs-injected and RGD-NRs-injected TBN mice (shown by blue arrows). These results showed the strongest toxicity of pure NRs and RGD-NRs on spleen, lung, and kidney during the tumor therapy. The tumor tissues were also collected after the tumor-therapy, and the H & E stained slices of pure NRs-injected and RGD-NRs-injected TBN mice showed no significant changes on their structures, compared with that of the physiological saline solution-

injected TBN mice, implying their non-effective therapy behavior on U251 tumor. However, a lot of cavities in the tumor slice of the RGD-NRs-CTX-injected TBN mice were emerged (shown by orange arrow), indicating the vast necrosis of tumor cells and their effective inhibition property on U251 tumor. In a word, the prepared RGD-NRs-CTX showed outstanding inhibition property on GBM, as well as good compatibility with normal organs and tissues.

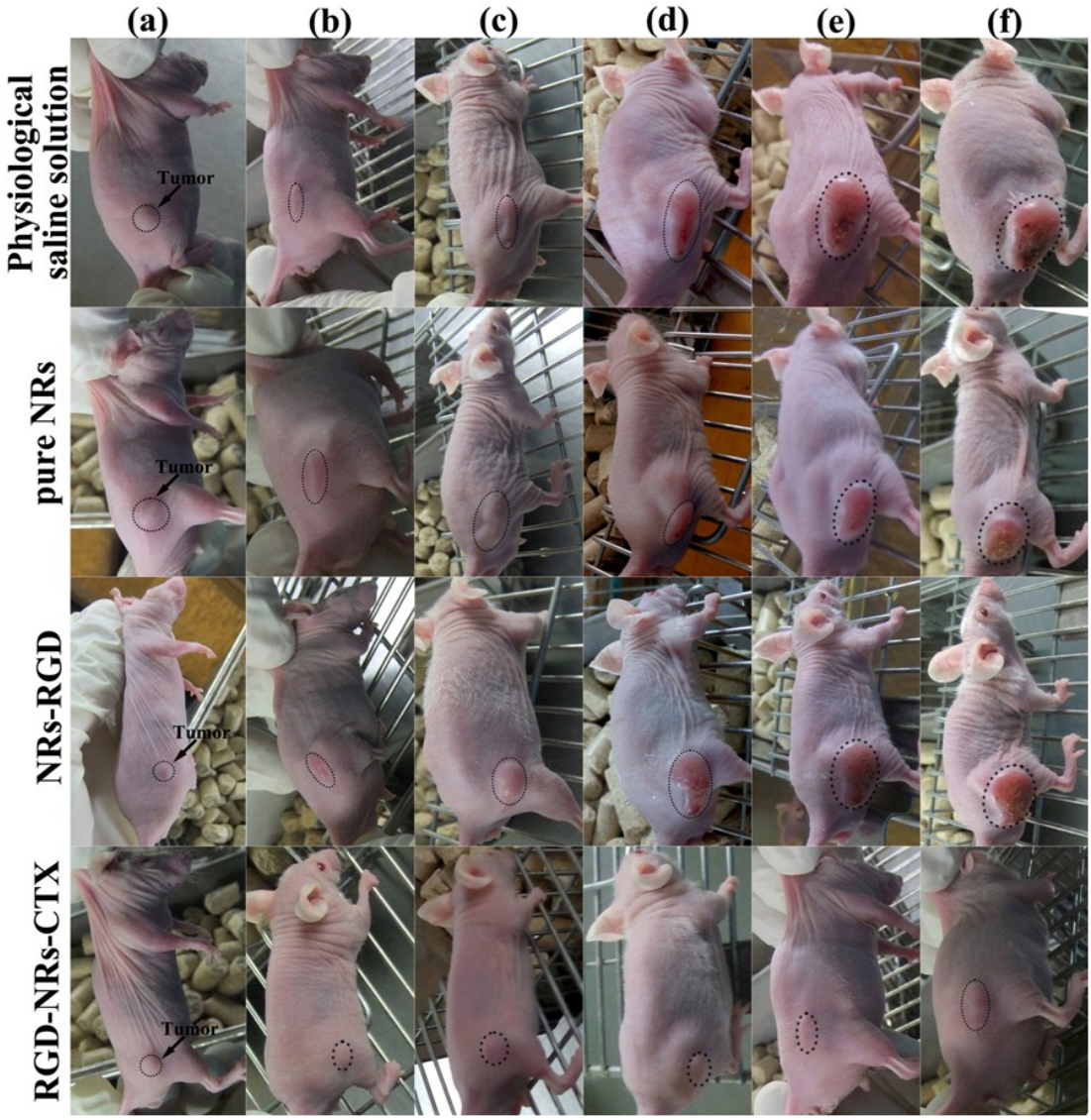

Fig. S18. Photographs of TBN mice after treated with physiological saline solution, pure NRs, RGD-NRs and RGD-NRS-CTX (photographs were taken each 5 d since the first time of treatment, 200 μL per day, 1 mg·mL^{-1}) for different time: (a) 0 (pre-injection), (b) 5, (c) 10, (d) 15, (e) 20 and (f) 25 d , respectively, after the first time of treatment.

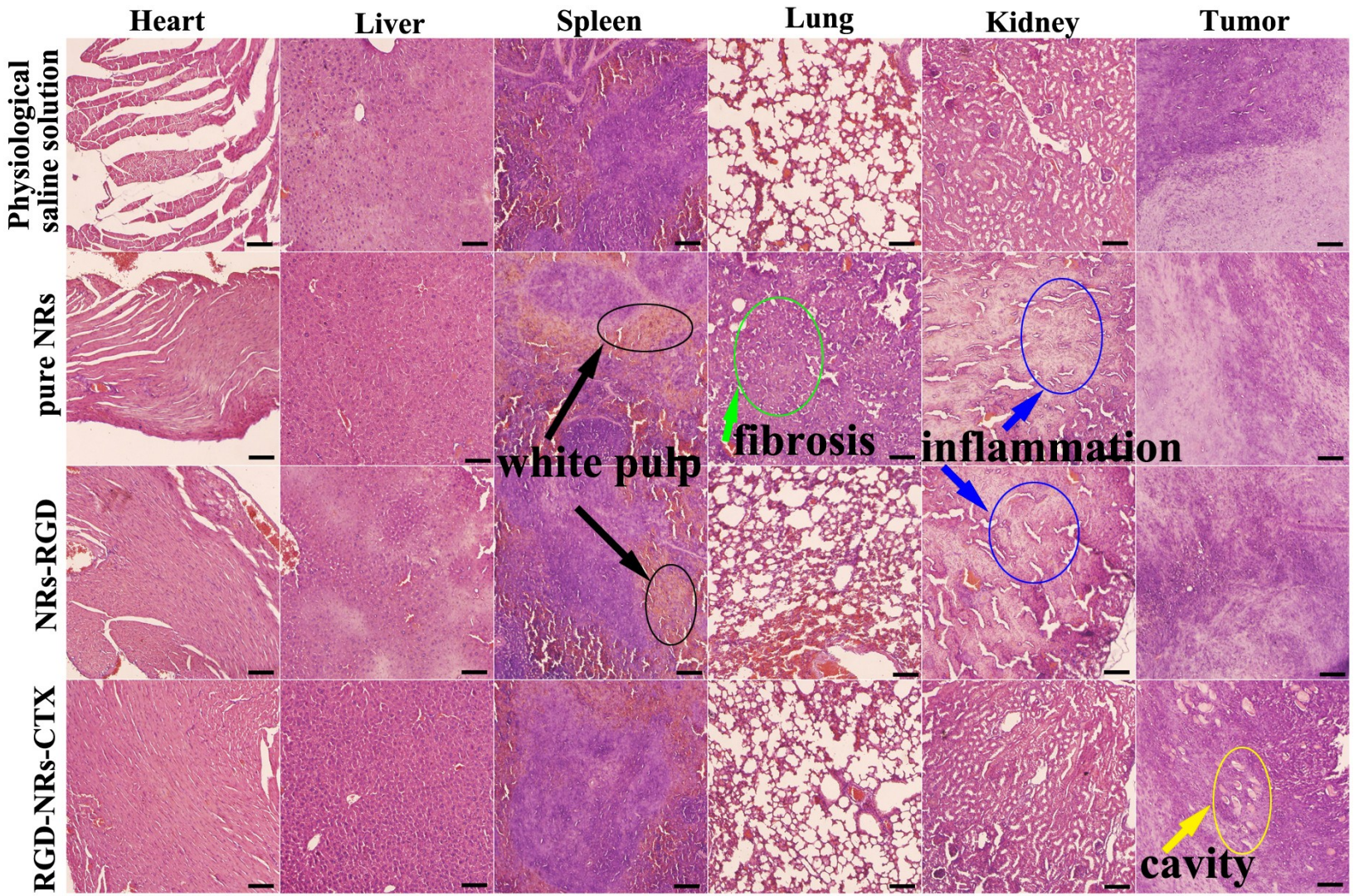

Fig. S19. The H & E-stained slices of heart, liver, spleen, lung, kidney and tumor from the TBN mice after treated with physiological saline solution, pure NRs, RGD-NRs and RGD-NRS-CTX (200 μL per day, 1 mg·mL^{-1}) for 25 d. Scale bars: 100 μm.

Reference

[1] Ying Lin, Wei Yao, Yuan Cheng, Hanqing Qian, Xin Wang, Yin Ding, et al. Multifold enhanced T_2 relaxation of $ZnFe_2O_4$ nanoparticles by jamming them inside chitosan nanospheres. J Mater Chem A. 2012; 22: 5684-93.

[2] Zhen Liu, Fang Pu, Sa Huang, Qinghai Yuan, Jinsong Ren, Qu X. Long-circulating Gd_2O_3:Yb^{3+}, Er^{3+} up-conversion nanoprobes as high-performance contrast agents for multi-modality imaging. Biomaterials. 2013; 34: 1712-21.

[3] Li Y, Chen T, Tan W, Talham DR. Size-dependent MRI relaxivity and dual imaging with $Eu_{0.2}Gd_{0.8}PO_4{\cdot}H_2O$ nanoparticles. Langmuir. 2014; 30: 5873-9.

[4] Qijun Du, Zhongbing Huang, Zhi Wu, Xianwei Meng, Guangfu Yin, Fabao Gao, et al. Facile preparation and bifunctional imaging of Eu-doped $GdPO_4$ nanorods with MRI and cellular luminescence. Dalton Trans. 2015; 44: 3934-40.

[5] Wu J, Zhou L, Ding X, Gao Y, Liu X. Biological Effect of Ultraviolet Photocatalysis on Nanoscale Titanium with a Focus on Physicochemical Mechanism. Langmuir. 2015; 31: 10037-46.

[6] Melanie B, Lilian K, Long NJ. Lanthanides in magnetic resonance imaging. Chemical Society Reviews. 2006; 35: 557-71.

[7] Guarnaccio A, D'Auria M, Racioppi R, Mattioli G, Bonapasta AA, De Bonis A, et al. Thiophene-Based Oligomers Interacting with Silver Surfaces and the Role of a Condensed Benzene Ring. J Phys Chem C. 2016; 120: 252-64.

[8] Richardson FS. Terbium (III) and Europium (III) Ions as Luminescent Probes and Stains for Biomolecular Systems. Chemical Reviews. 1982; 82: 541-52.

[9] Peng C, Zheng L, Chen Q, Shen M, Guo R, Wang H, et al. PEGylated dendrimer-entrapped gold nanoparticles for in vivo blood pool and tumor imaging by computed tomography. Biomaterials. 2012; 33: 1107-19.

[10] Yi Z, Lu W, Xu Y, Yang J, Deng L, Qian C, et al. PEGylated $NaLuF_4$: Yb/Er upconversion nanophosphors for *in vivo* synergistic fluorescence/X-ray bioimaging and long-lasting, real-time tracking. Biomaterials. 2014; 35: 9689-97.

[11] Rammohan A, Mishra G, Mahaling B, Tayal L, Mukhopadhyay A, Gambhir S, et al. PEGylated Carbon Nanocapsule: A Universal Reactor and Carrier for In Vivo Delivery of Hydrophobic and Hydrophilic Nanoparticles. ACS Appl Mater Interfaces. 2016; 8: 350-62.

[12] Mansouri S, Merhi Y, Winnik FM, Tabrizian M. Investigation of layer-by-layer assembly of polyelectrolytes on fully functional human red blood cells in suspension for attenuated immune response. Biomacromolecules. 2011; 12: 585-92.

[13] Slowing, II, Wu CW, Vivero-Escoto JL, Lin VS. Mesoporous silica nanoparticles for reducing hemolytic activity towards mammalian red blood cells. Small. 2009; 5: 57-62.

[14] Yu-Shen Lin, Haynes CL. Impacts of Mesoporous Silica Nanoparticle Size, Pore Ordering, and Pore Integrity on Hemolytic Activity. J Am Chem Soc 2010; 132: 4834-42.

[15] Ai K, Liu Y, Liu J, Yuan Q, He Y, Lu L. Large-scale synthesis of Bi_2S_3 nanodots as a contrast agent for in vivo X-ray computed tomography imaging. Adv Mater. 2011; 23: 4886-91.

[16] Liu Y, Ai K, Liu J, Yuan Q, He Y, Lu L. A high-performance ytterbium-based nanoparticulate contrast agent for in vivo X-ray computed tomography imaging. Angewandte Chemie. 2012;

51: 1437-42.
[17] Xiong L, Yang T, Yang Y, Xu C, Li F. Long-term in vivo biodistribution imaging and toxicity of polyacrylic acid-coated upconversion nanophosphors. Biomaterials. 2010; 31: 7078-85.
[18] Yang Yang, Yun Sun, Ying Liu, Juanjuan Peng, Yongquan Wu, Yingjian Zhang, et al. Long-term in vivo biodistribution and toxicity of $Gd(OH)_3$ nanorods. Biomaterials. 2013; 34: 508-15.